Materials Science & Engineering A 733 (2018) 87–97

Contents lists available at ScienceDirect

Materials Science & Engineering A

journal homepage: www.elsevier.com/locate/msea

Recrystallization behavior in a low-density high-Mn high-Al austenitic steel undergone thin strip casting process

Fengqin Ji[a,b,*], Wenwen Song[b], Yan Ma[b], Chengning Li[c], Wolfgang Bleck[b], Guodong Wang[a]

[a] State Key Laboratory of Rolling and Automation, Northeastern University, Shenyang 110819, China
[b] Department of Ferrous Metallurgy, RWTH Aachen University, Aachen 52072, Germany
[c] School of Materials Science and Engineering, Tianjin University, Tianjin 300350, China

ARTICLE INFO

Keywords:
Recrystallization
High-Mn steel
Lightweight steel
Grain size
Strain hardening behavior
Toughness

ABSTRACT

The recrystallization behavior of a high-Mn high-Al lightweight steel (Fe-28.4Mn-8.3Al-1.27 C (wt%)) with 50% cold rolling deformation is investigated at the annealing temperature of 800 °C, 900 °C and 1000 °C. The detailed microstructure evolution is characterized by optical microscopy (OM), scanning electron microscopy (SEM), electron backscatter diffraction (EBSD), X-ray diffraction (XRD), electron probe micro-analyzer (EPMA) and transmission electron microscopy (TEM). The partial recrystallized bimodal austenite grains and κ-phase $(Fe, Mn)_3AlC$ form at 800 °C, while fully recrystallized austenite grains without κ-phase appear at 900 °C and 1000 °C. With the increase in annealing temperature, the increased frequency of annealing twin boundaries reduces the average austenitic grain size and the dispersion of the austenite grain size effectively. The effect of austenite grain size on the tensile properties is discussed. The strain hardening behavior is also investigated by Hollomon analysis and C-J analysis, and the later one is better to explain the strain hardening behavior in different four stages. The recrystallization behavior significantly improves the tensile toughness from 59 MJ/m^3 to 436 MJ/m^3 at the expense of tensile strength decrease from 1460 MPa to 890 MPa, due to the homogenous fine austenite grains and high frequency of high misorientation angle. The steel with fully recrystallized austenite grains of 10.0 μm annealed at 900 °C exhibits the optimum mechanical properties with excellent tensile strength of 965 MPa, ductility of 48.3%, and good toughness of 400 MJ/m^3.

1. Introduction

The lightweight Fe-Mn-Al-C steels have drawn much attention in recent years for the application in automotive industry, due to their excellent mechanical properties and low-density potential [1–11]. According to the chemical composition, Fe-Mn-Al-C steels can be classified into ferritic steels, duplex steels and austenitic steels [3]. Austenitic steels containing a high Mn content of 12–20 wt%, high Al content of 5–12 wt% and 0.6–2 wt% C content are the most attractive for material researchers due to their extraordinary tensile properties and superior strain hardening behavior [7]. This type of steels has two states: aged and non-aged.

For the aged austenitic Fe-Mn-Al-C steels, κ-phase precipitation hardening is a significant strengthening method, and the related work about κ-phase precipitation behavior and strain hardening mechanisms have been intensively studied [12–34]. The nano-sized intragranular κ-phase strengthening can provide high yield strength of 800–1200 MPa and good ductility of 30–50% [12–14], while the intergranular κ-phase precipitation controls the toughness and leads to low ductility [7], depending on the chemical composition, aging temperature and aging time [15–18]. The deformation mechanism in the lightweight high-Mn high-Al steels is controversially discussed in previous studies. Yoo et al. [19,20] reported that the formation of microbands contributes to the excellent plasticity and high strength in Fe-28Mn-9Al-0.8 C alloy and Fe-28Mn-10Al-1.0 C alloy, named microband induced plasticity (MBIP). However, the work from Choi et al. [12] reported less tensile elongation with the same steel composition of Fe-28Mn-9Al-0.8 C and explained the plastic deformation behavior with the formation of planar slip bands related to the shearing of κ-phase by dislocations. The deformation mechanism of Fe-30.4Mn-8Al-1.2 C steel was also investigated with two states: solution treatment at 1100 °C for 2 h and annealed at 600 °C for 24 h [21,22]. The deformation microstructure observed by electron channeling contrast imaging (ECCI) indicated the formation and refinement of planar slip bands with the increasing of true strain, regarded as dynamic slip band refinement (DSBR). For non-aged austenitic Fe-Mn-Al-C steels, short-range ordering (SRO) clusters

* Corresponding author at: State Key Laboratory of Rolling and Automation, Northeastern University, Shenyang 110819, China.
E-mail address: jifqin@sina.com (F. Ji).

https://doi.org/10.1016/j.msea.2018.07.023
Received 9 March 2018; Received in revised form 8 July 2018; Accepted 9 July 2018
Available online 10 July 2018
0921-5093/

[22–25] in the solution state also contribute to planar glide and has the same restriction influence on the interaction of dislocations as κ-phase, called 'glide plane softening' [35]. These proposed mechanisms are suitable for the explanation of strengthening mechanism for both aged and non-aged Fe-Mn-Al-C steels [19–23].

Grain size refinement is also an important strengthening mechanism [36–38], especially for non-aged Fe-Mn-Al-C steels. The recrystallization annealing combined with cold rolling is a very effective approach for the austenitic grain size refinement, since most of the automobile steels with thin gauge are produced by cold rolling and subsequent annealing [39–42]. Thus, recrystallization behavior is an important factor to control the mechanical properties. Although many literatures focus on the isothermal control of κ-phase precipitation and the related strain hardening mechanisms on the precipitation-hardened steels, the investigation on the recrystallization behavior for the non-aged Fe-Mn-Al-C austenitic steels is inadequate, especially for the steels produced by thin strip casting process.

In the present study, the purpose is to clarify the recrystallization behavior in such material produced by thin strip casting process and 50% cold rolling deformation. SEM and EBSD techniques are employed to characterize the microstructure evolution at different annealing temperature. The combination of XRD, TEM and EPMA focuses on the phase constitutes and κ-phase precipitation during the annealing process. The austenite grain size effects on the mechanical properties and the strain hardening rate are discussed. In addition, the tensile toughness is also analyzed according to the related fracture surface and tensile strength.

2. Experimental procedure

The investigated material in this work is high-Mn high-Al steel produced by thin strip casting process. The exact chemical composition determined by wet chemical analysis method is Fe-28.4Mn-8.3Al-1.27C-0.25Si-0.01S-0.01 N (wt%). The density of the investigated material was measured to be 6.75 g/cm^3 by Micromeritics gas pycnometer (AccPyc Pyknometer 1330), 14.2% lower than the conventional steels with density of 7.87 g/cm^3. According to the subregular solution thermodynamic model [43], the stacking fault energy (SFE) of this steel was calculated to be about 88.4 mJ/m^2. In order to determine appropriate recrystallization annealing temperature, the equilibrium phase fraction as a function of temperature for the investigated material was calculated using the Thermo-Calc software [44] and Hallstedt database [4], shown in Fig. 1. It indicates that the κ-phase (KAPPA_E21) emerges below 805 °C, thus the recrystallization annealing temperature here is set to 800 °C, 900 °C and 1000 °C, respectively.

The schematic material preparation process is presented in Fig. 2. The material was melt under Ar atmosphere and strip cast into sheets with 2.0 mm thickness through twin-roll strip casting machine at the Institute of Metal Forming (IBF) of RWTH Aachen University. To moderate the as-cast dendrites and the chemical segregation, the sheets covered with protective foil were reheated to 1150 °C for 5 h in Ar atmosphere and subsequently water quenched to room temperature. In order to study the recrystallization behavior, the sheets were cold rolled to 1.0 mm thickness with 50% reduction to provide driving force of recrystallization. The subsequent recrystallization annealing was carried out at 800 °C, 900 °C and 1000 °C for 20 min, respectively. For the convenience of description in the following sections, they are termed as state 800, state 900 and state 1000, respectively.

The microstructure evolution of strip cast state, homogenization state, and cold-rolled state with different recrystallization annealing heat treatment was observed using an optical microscope (OM). The metallographic specimens for OM observation were color etched in LB-Ätzung solution. A field emission scanning electron microscope (FE-SEM, Zeiss SIGMA) combined with Oxford electron backscatter diffraction (EBSD) and energy dispersive X-ray spectroscopy (EDX) was used to perform the further microstructure analysis. The specimens for

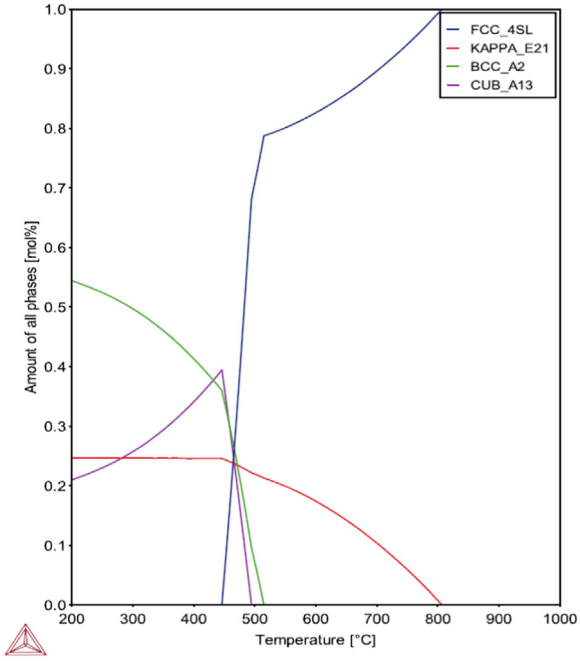

Fig. 1. Equilibrium phase fraction of the investigated material as a function of temperature.

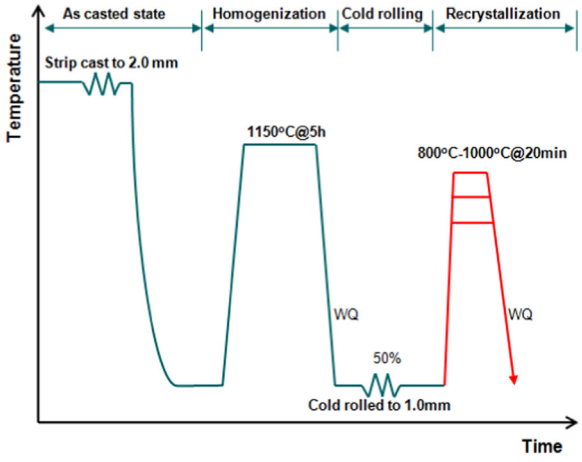

Fig. 2. Schematic process of the investigated material after thin strip casting, in order to study the recrystallization behavior.

SEM observation were etched in a solution with 5% Nital for 15 min at room temperature. The specimens for EBSD analysis were electro-polished using a Struers A2 electrolyte with about 85% ethanol, 10% 2-butoxyethanol and 5% water for 15 s at 30 V. The EBSD measurements were operated at a voltage of 20 kV to scan areas of 600 μm × 450 μm with a step size of 1 μm. The characterization of OM, SEM and EBSD techniques was performed on the rolling direction (RD) plane, i.e. the plane which is perpendicular to the rolling direction.

The EBSD data analysis was carried out using *HKL* Channel-5 software. The grain boundary distribution and Kernel average misorientation (KAM) [39] of the substructure were obtained to determine the recrystallization behavior. Low angle grain boundaries (LAGBs) were defined as the misorientation angles ranging from 2° to 10°, and high angle grain boundaries (HAGBs) were defined as the misorientation angles higher than 10°, including the twin boundaries (TBs) ($\Sigma3 = 60^\circ < 111 >$). The boundaries with misorientation angles smaller than 2° were ignored to remove the inaccurate points. Misorientation angle distributions of different annealing states were

obtained to discuss the relationship between grain boundaries and toughness.

X-ray diffraction (XRD) patterns were measured on the normal direction (ND) plane (the plane which is perpendicular to the normal direction) with power diffractometer Stadi MP at room temperature in the range of 5°-85° with Mo K_α radiation source and step size of 0.015° (2Theta) to characterize the phase constituents before and after the recrystallization annealing. In addition, electron probe micro-analyzer (EPMA) was also applied to acquire the 2D element maps of the elements distribution.

Detailed microstructural characterization were performed with a field-emission transmission electron microscopy (TEM, FEI Tecnai G^2) equipped with energy dispersive X-ray spectroscopy (EDX) at 200 kV. The samples were ground mechanically to 50 μm in thickness, punched into disks of a diameter 3 mm, and then twin-jet polished in an electrolyte containing 8% perchloric acid and 92% ethyl alcohol at −30 °C.

Tensile tests were performed with a constant strain rate of 1×10^{-3} s^{-1} at room temperature in a Zwick-100 tensile machine. According to DIN EN ISO 6892-1, the flat tensile samples were prepared perpendicular to the rolling direction, with the dimension of gauge length 20 mm and width 6 mm. After tensile tests, the fracture surfaces were observed using FE-SEM with EDX and the fractographic images combined with the misorientation angle distribution were also discussed.

3. Results

3.1. Initial microstructure

The initial microstructural images after strip casting, homogenization at 1150 °C for 5 h and cold rolling process are shown in Fig. 3. The dendritic structure nucleated at the interface between the casting strip and the cooled casting rolls and grew towards the strip center reaching up to 800 μm during strip casting, and the columnar dendrites stopped to grow and partially broken at the front, shown in the inset of Fig. 3a. The strip center area has pronounced Mn element microsegregations, shown in Fig. 3g–h. The homogenization after strip casting eliminates the dendritic structure and forms large long grains along the normal direction and small equiaxed grains along with annealing twinning (Fig. 3b). Homogenization annealing can easily dissolve microsegrations [45]. Compared with cast strip, both deviation and wavelength of the Mn element after homogenization at 1150 °C for 5 h decrease, shown in Fig. 3h.

In the inset of Fig. 3c, numerous deformation bands exist in the deformed austenitic grains after the 50% reduction in cold rolling process, which provide the driving force for further recrystallization behavior. SEM observation of the cold rolled sample shows the deformation bands along two principal directions in a grain and appear wavy in some areas, shown in Fig. 4**a**, and they depict the narrow localized deformed areas at the macroscopic scale. Details of the deformation bands are analyzed using TEM, shown in Fig. 4**b–c**. It presents intensive refined slip bands with a high density of dislocations along {111} slip plane, and their bandwidth is about 60 nm. The deformation is typical planar dislocation glide. With the increase in strain, the dislocation sources are activated first and then emit dislocations on the slip planes; the slip planes filled with dislocations appear as slip bands throughout the grain. Subsequently, more dislocation sources are activated to accommodate further plastic strain and stimulate the formation of new slip bands, leading to the reduced spacing between slip bands during plastic deformation. This phenomenon is called the dynamic slip bands refinement (DSBR), resulting in high continuous strain hardening. The results shown in Fig. 4 resemble those in ref. [22].

3.2. Recrystallized microstructure

The optical microstructure images of recrystallization annealed samples are shown in Fig. 3d-f. For state 800, the fraction of recrystallized grains accounts for 80%, and non-recrystallized grains still exist within the dot lines. It indicates that the microstructure at annealing temperature 800 °C is partial recrystallization. The microstructure of state 900 and state 1000 is fully recrystallized grains, and the grain size is increased with the increase in annealing temperature.

The EBSD boundary maps of the material with different states are shown in Fig. 5. Low angle grain boundaries (LAGBs), high angle grain boundaries (HAGBs) and twin boundaries with $\Sigma3 = 60^\circ < 111 >$ coincidence orientation relationship are plotted by green lines, black lines and red lines, respectively. For the cold-rolled state, the large elongated austenitic grains with diameter about 200 μm are full of LAGBs, observed in Fig. 5a. For state 800, the microstructure exhibits a bimodal structure: ultra-fine recrystallized grains and some large non-recrystallized grains within dense LAGBs, shown in Fig. 5b. It indicates that partial recrystallization causes severe inhomogeneous grains size distribution. For state 900, the microstructure is fully recrystallized fine austenite grains with the annihilation of LAGBs, shown in Fig. 5c. For state 1000, the fully recrystallized microstructure shows coarse equiaxed grains. Most of the recrystallized grains contain abundant annealing twin boundaries [46], similar results are also obtained in Fig. 5c-d.

Due to the existence of twin boundaries, two different average grain sizes have been measured: the grain size without considering twin boundaries and the grain size considering twin boundaries, shown in Fig. 6. The austenitic grain size distribution without considering twin boundaries is more scattered than that of considering twin boundaries (Fig. 6a). The statistics of Σ3 twin boundary frequency in Fig. 5b-d is 29%, 39% and 49% at the annealing temperature of 800 °C, 900 °C and 1000 °C, respectively. When the twin boundaries are considered, the average austenitic grain size increases from 7.0 μm to 10.0 μm and finally to 21.2 μm with the annealing temperature increase from 800 °C to 1000 °C; on the other hand, the average austenite grain size increases from 8.5 μm to 16.3 μm and finally to 44.0 μm without considering twin boundaries. The annealing twin boundaries effectively reduce the average austenitic grain size and the dispersity of the austenitic grain size. In the following sections, the mentioned average austenitic grain size is regarded as the austenite grain size considering twin boundaries.

In order to distinguish the initial deformed grains and the recrystallized grains, the KAM maps are also obtained from the EBSD measurements for different states, shown in Fig. 7. The degree of misorientation related to the stored strain energy [47] is presented with different colors. Most of the green areas with KAM higher than 2° correspond to high stored energy area with high density of geometrically necessary dislocations (GNDs) [48], shown in Fig. 7a–b, and the recovery and recrystallization lead to approximately zero local misorientation due to the annihilation and rearrangement of GNDs. The high annealing temperature is beneficial for fully recrystallization and relaxation of the stored energy, shown in Fig. 7d. The similar results were also found in the ref. [49].

The misorientation angle distribution of samples with different states is shown in Fig. 8. It demonstrates that most of the grain boundaries in the samples with different annealing temperature are high misorientation angles, and this phenomenon reveals the recrystallization behavior [36]. The relative frequency of small misorientation angle in the cold-rolled state is higher than that of other states; on the other hand, the relative frequency of high misorientation angle (especially above 55°) increases with the increase in annealing temperature, which is related to the high toughness due to the large energy consumption for crack propagation encountered large-angle grain boundaries [50].

3.3. Carbide precipitation

Fig. 9 shows the SEM images of particles in the samples annealed at 800 °C and 900 °C, respectively. The white particles precipitated in state 800 have three different morphologies. The first type is spherical

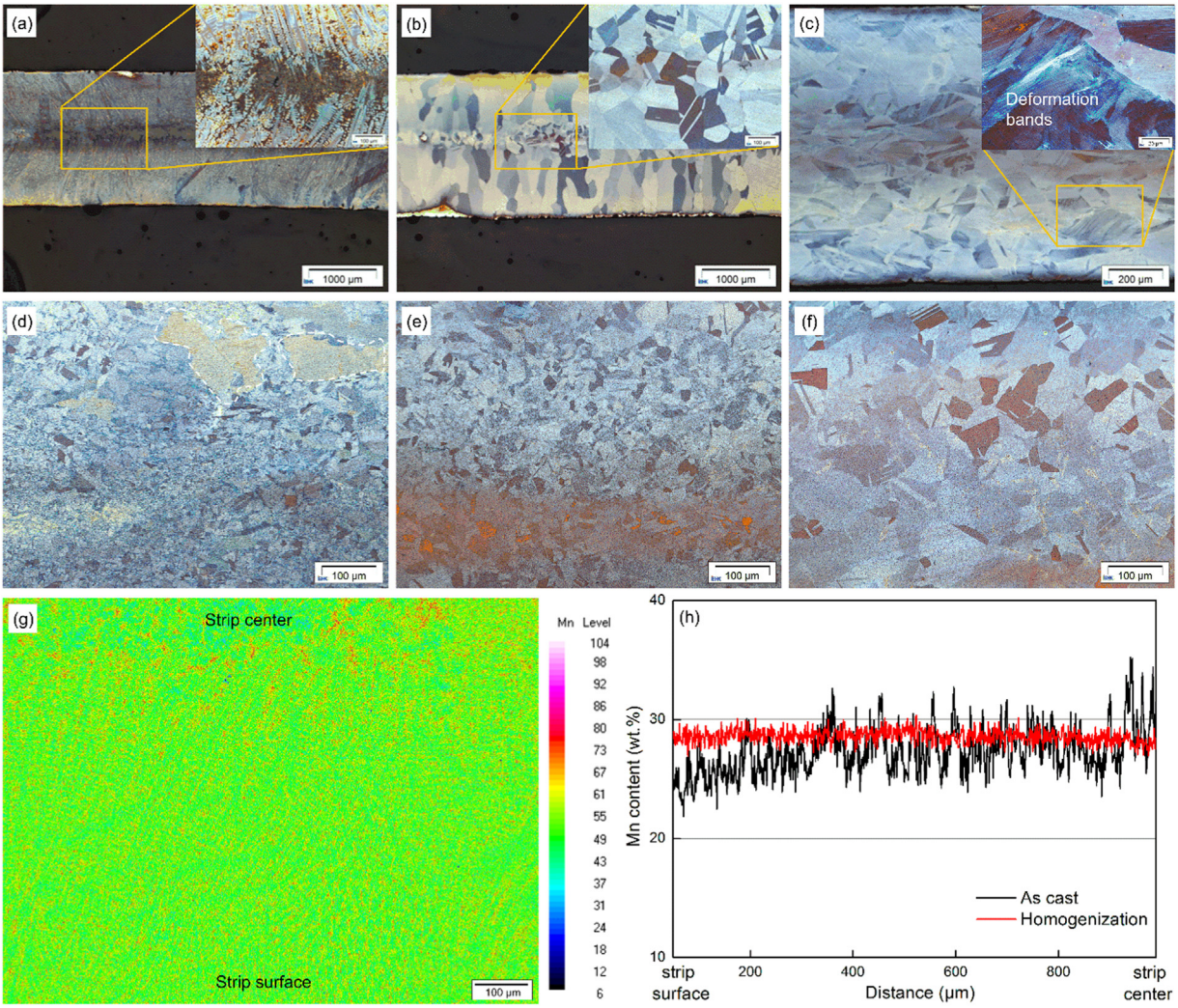

Fig. 3. Optical images and elemental analysis of steel under different processing conditions: (a) strip casting, (b) homogenization at 1150 °C for 5 h, (c) cold rolling with 50% reduction, (d) state 800, (e) state 900, (f) state 1000, (g) element mapping of Mn in (a), and (h) concentration profiles of Mn in the cast strip (black line) and homogenization strip (red line). (For interpretation of the references to color in this figure legend, the reader is referred to the web version of this article.).

particles with size about 2 μm distributed at the grain boundaries (depicted in Fig. 9a), the second type is spherical particles with the size less than 2 μm inside the grains (Fig. 9b), and the third type is needle-like particles of 4 μm distributed within the austenite grains adjacent the grain boundaries (Fig. 9b–c). According to the EDX analysis results, the atomic mass ratio of particle A in the red circle in Fig. 9a is C: Al: Mn: Fe = 17.01: 10.69: 29.39: 42.50, while the atomic mass ratio of the austenitic matrix in the green circle B is C: Al: Mn: Fe = 6.21: 8.31: 29.05:

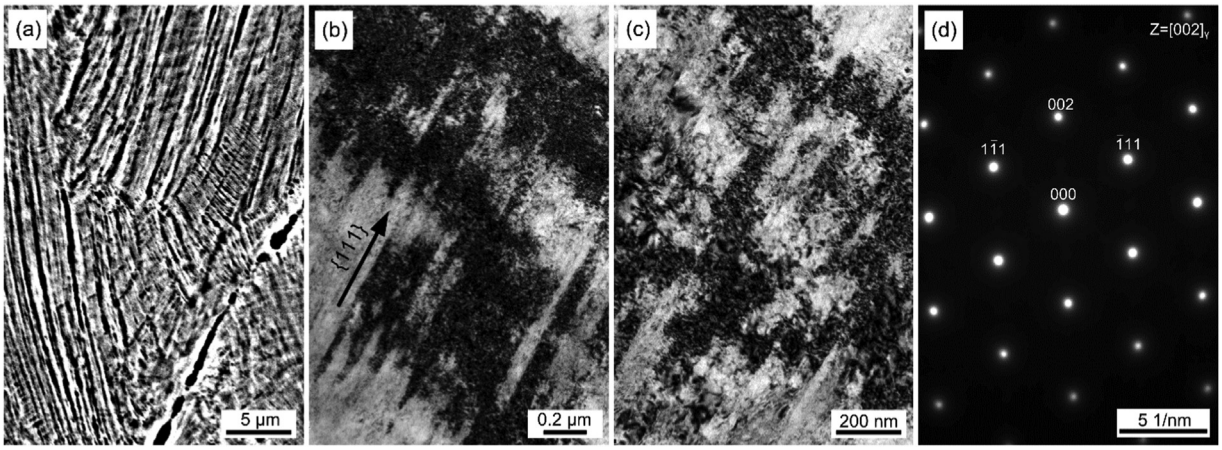

Fig. 4. (a) SEM image, (b–c) TEM high magnification images of deformation bands in the 50% cold rolled steel and (c) the corresponding selected area electron diffraction pattern.

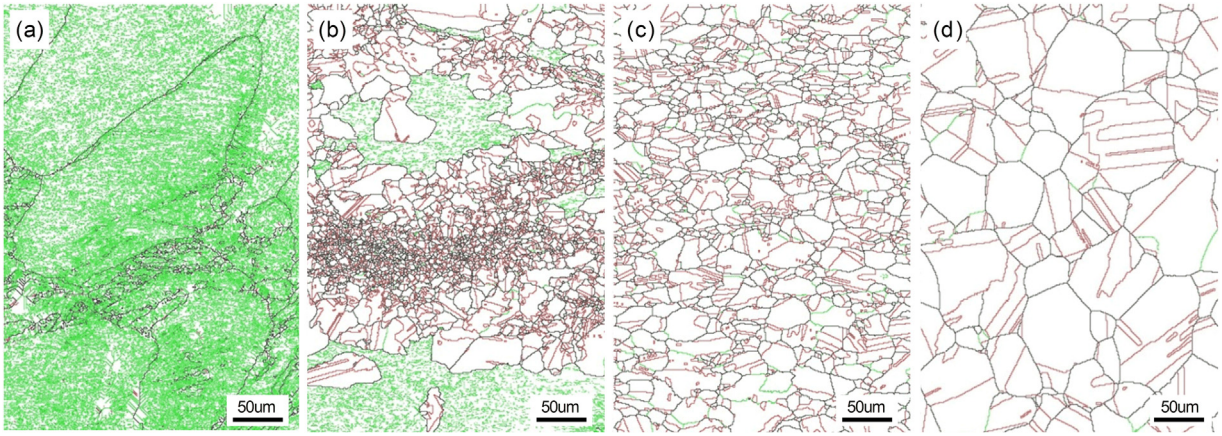

Fig. 5. EBSD boundary maps of the material with different states: (a) cold-rolled state, (b) state 800, (c) state 900 and (d) state 1000. The LAGBs, HAGBs, and Σ3 boundaries are plotted as green lines, black lines and red lines, respectively. (For interpretation of the references to color in this figure legend, the reader is referred to the web version of this article.).

56.35. It indicates that the carbon content and Al content of the particles are much higher than that of the matrix, while the Mn content is comparable. In addition, the EPMA results in Fig. 9e-f also exhibit higher C and Al contents of the particles, which are consistent with the EDX analysis results. The similar result obtained by atom probe tomography (APT) is also reported in ref. [21]. The material annealed at 900 °C does not manifest the white particles, and there are only a few AlN/ MnS inclusions observed within the matrix.

The X-ray diffraction (XRD) diagrams of the investigated material with different states are depicted in Fig. 10. The diffraction result shows austenitic peaks in the cold-rolled sample, state 900 and state 1000. However, the XRD result of state 800 displays small peaks (111) and (200) of kappa phase additionally with a lattice constant of 0.3778 nm, shown in Fig. 10a. It indicates that the white particles in Fig. 9a-c is κ-phase $(Fe, Mn)_3AlC$ precipitated at the annealing temperature of 800 °C. The XRD result is consistent with the SEM result in Fig. 9 and the calculated Thermo-Calc result in Fig. 1. In addition, the austenitic peaks slightly shift to the lower angle with the increase in annealing temperature, shown in Fig. 10b. It indicates that the lattice constant increases with the annealing temperature, since high temperature promotes the elemental solution into the crystal lattice [51]. It should be noted that every austenite peak splits into two peaks here, probably because the inhomogeneous microstructures stemmed from strip casting process lead to carbon-enriched austenite grains and carbon-depleted austenite grains. The similar phenomenon was also found in the work studied by in-situ synchrotron X-ray diffraction [52,53].

Fig. 11 shows the detailed TEM dark field micrographs of the microstructure in the annealed samples. It is found that very fine coherent ordered clusters about 1 nm distribute uniformly within the austenite matrix in the samples annealed at 800 °C, 900 °C and 1000 °C, respectively. The intensity of these superlattice reflections is very low and indicates a low volume fraction of precipitates. Since the significant elemental partitioning is not possible during quenching, full κ-carbide formation is unlikely to occur [22]. The high temperature austenite decomposes into low temperature solute-rich austenite and solute-lean austenite and the former one transforms into the ordered $L`1_2$ phase via ordering reaction [24].

3.4. Mechanical properties

The tensile engineering stress-strain curves of the samples with different states are shown in Fig. 12. The cold-rolled sample exhibits the highest tensile strength of 1460 MPa and the smallest elongation of 4.5%. After recrystallization annealing, the strength reduces and the elongation rises with the increase in annealing temperature. The yield strength (YS), ultimate tensile strength (TS) and total elongation (EL) are plotted against the annealing temperature in Fig. 12b. For state 800, the ultimate tensile strength is 1050 MPa with the total elongation of 24.5%. For state 900, the ultimate tensile strength reduces to 965 MPa and the elongation rises up to 48.3%. For state 1000, the ultimate

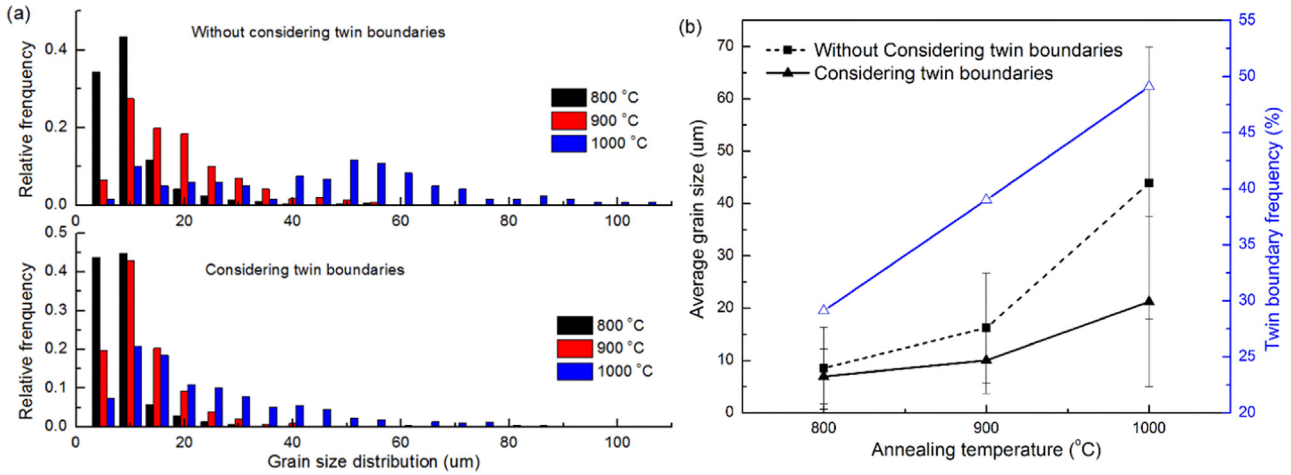

Fig. 6. (a) Relative frequency of grain size distribution with and without considering twin boundaries, and (b) variation of the average austenitic grain size and the twin boundary frequency with the annealing temperature.

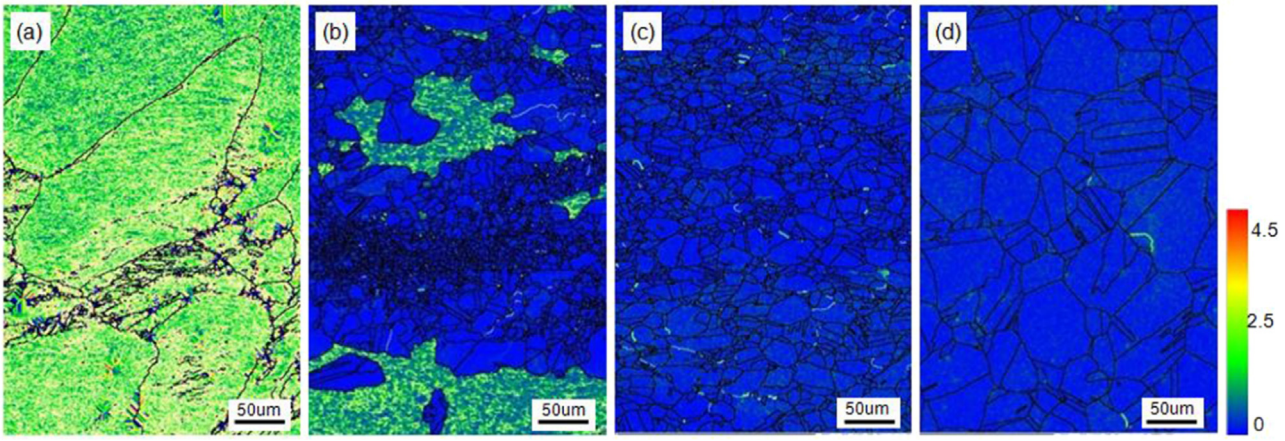

Fig. 7. KAM maps and EBSD grain boundary maps as a function of annealing temperature: (a) cold-rolled state, (b) 800 °C, (c) 900 °C and (d) 1000 °C. The LAGBs and HAGBs are plotted as green lines, and black lines, respectively. (For interpretation of the references to color in this figure legend, the reader is referred to the web version of this article.).

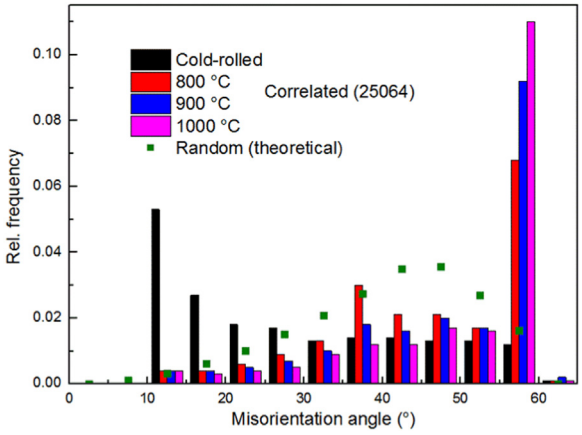

Fig. 8. Misorientation angle distribution of samples with different annealing states obtained by EBSD technique.

tensile strength drops to 890 MPa and the elongation increases to 57.8%. On the other hand, the yield strength is also decreased with increase in annealing temperature, which is related to the dislocation annihilation and grain coarsening. Moreover, the gap between yield strength and tensile strength gradually increases with the increase in annealing temperature. Consequently, the product of ultimate tensile strength and total elongation increases roughly from 25.7 GPa·% to 46.6 GPa·% and 51.4 GPa·% when the annealing temperature increases from 800 °C to 1000 °C.

From the tensile results shown in Fig. 12, the refined austenite grain size enhances the yield strength and ultimate tensile strength. The Hall-Petch relationship, $\sigma = \sigma_0 + k/d^{-0.5}$ [38] for the yield strength and ultimate tensile strength is calculated according to the fully re-crystallized samples, respectively.

$$\sigma_y = 319 + 811/d^{-0.5} \quad (1)$$

$$\sigma_t = 725 + 760/d^{-0.5} \quad (2)$$

where σ_y is yield strength, σ_t is ultimate tensile strength, and d is the

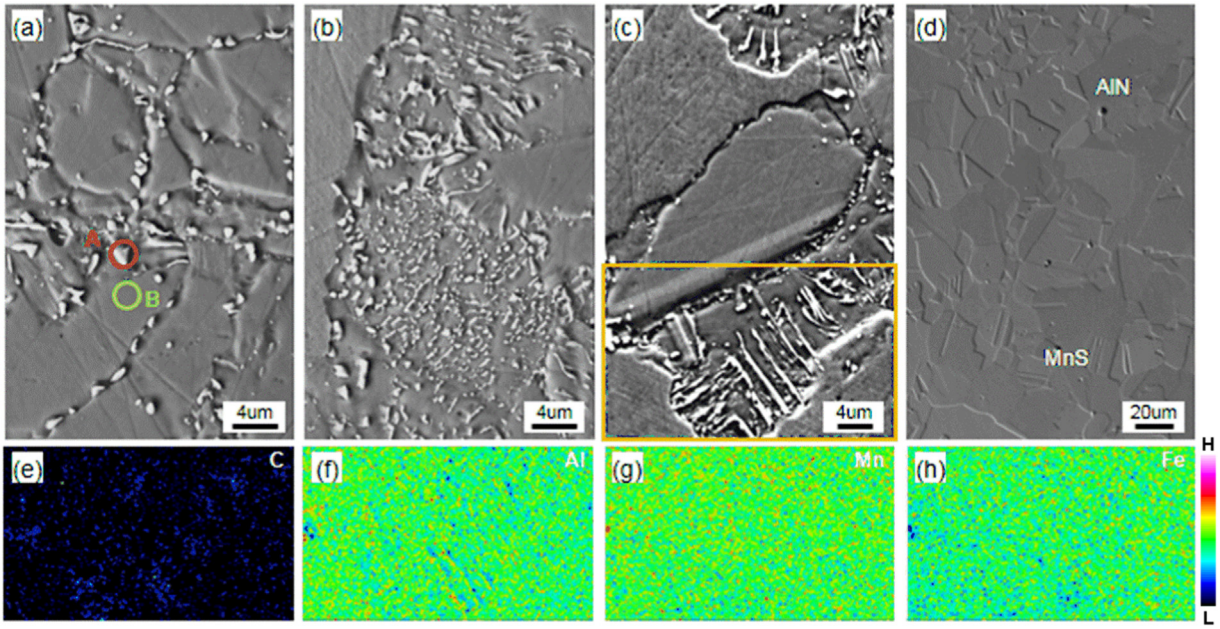

Fig. 9. SEM micrographs showing the carbides in the samples at state 800 (a–c) and state 900 (d), and EPMA element distribution maps presenting the C, Al, Mn and Fe distributions (e–h) of carbides within the orange frame section in (c).

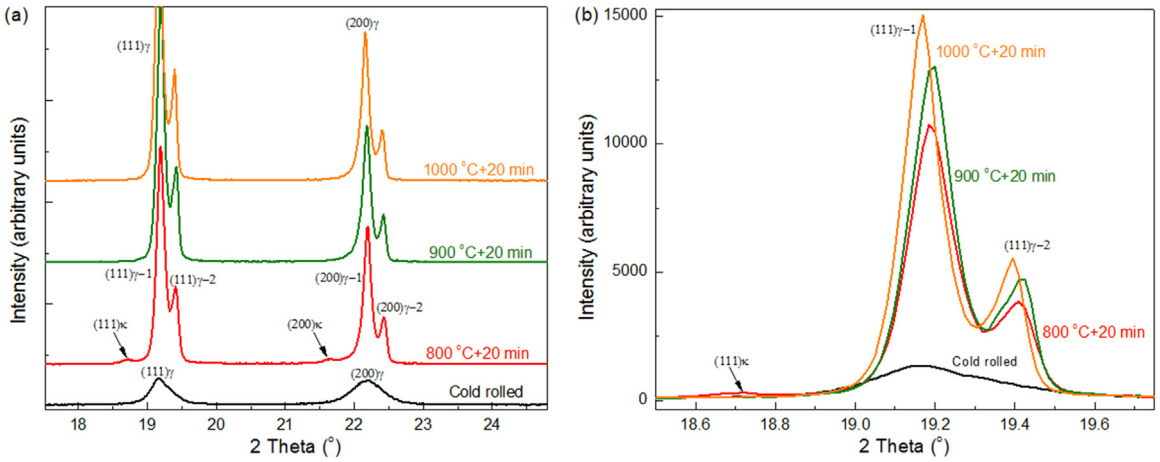

Fig. 10. X-ray diffraction diagrams of the investigated material in the state CR (cold-rolled) and with different recrystallized temperatures: state 800, state 900 and state 1000.

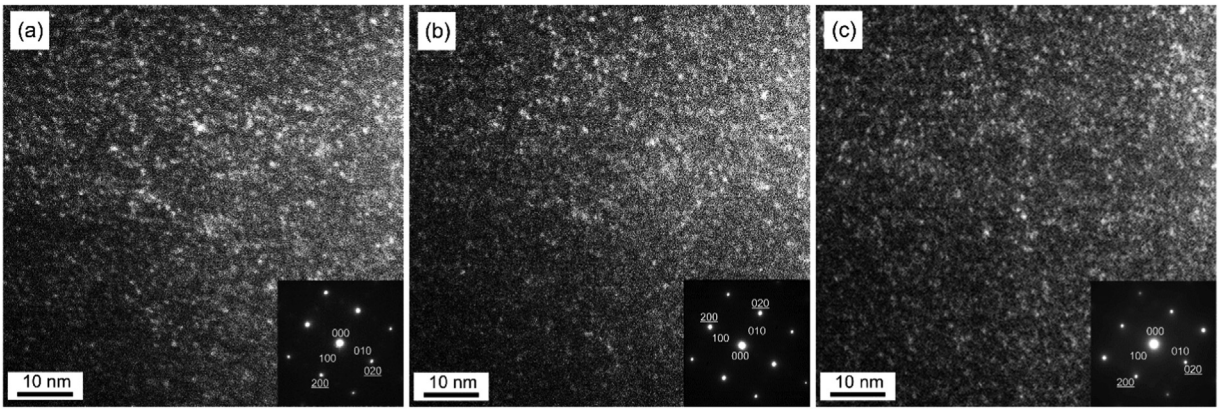

Fig. 11. TEM dark field micrographs of the investigated material in the (a) state 800, (b) state 900 and (c) state 1000.

average austenitic grain size considering twin boundaries.

The values of initial strength and Hall-Petch parameter k are different from those obtained in the ref. [37], which may be due to the difference of austenite grain size and chemical composition. The refinement of austenitic grain size considering the twin boundaries can effectively block the dislocation motion and provide strengthening [54]. When the recrystallized austenite grain size is larger than 10 μm, the total elongation significantly promotes to 48.3% and even 57.8%. The total elongation increased with the increase in austenite grain size was also reported in ref. [20,38]. Comparing all the results, the state 900 with fully recrystallized grains exhibits the optimum mechanical properties with excellent strength of 965 MPa and ductility of 48.3%. The control of austenite grain size through recrystallization behavior is important to obtain the balance of strength and ductility.

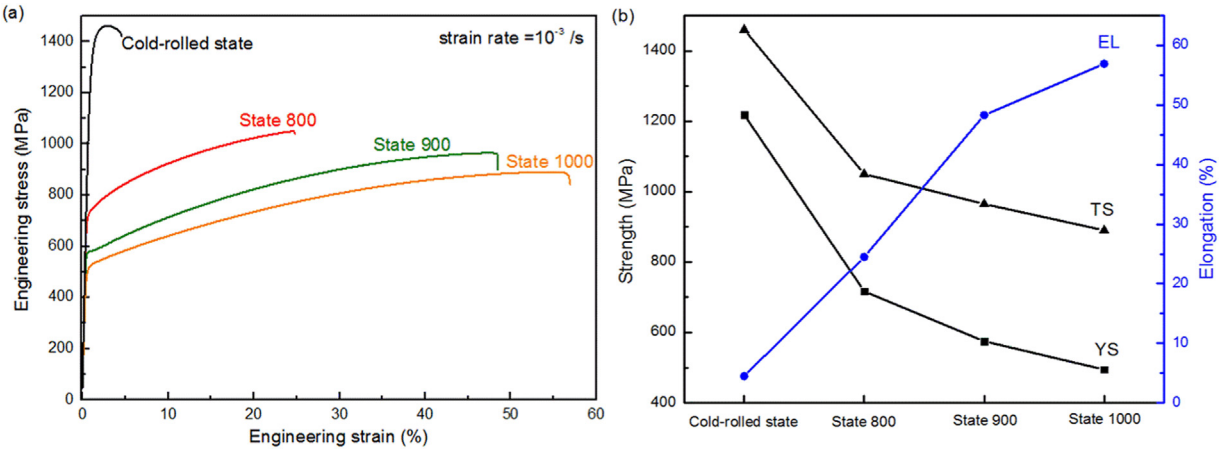

Fig. 12. (a) Engineering stress-strain curves of the cold-rolled and annealed samples at 800–1000 °C for 20 min, and (b) changes in strength and elongation with the annealing temperature of the investigated steel.

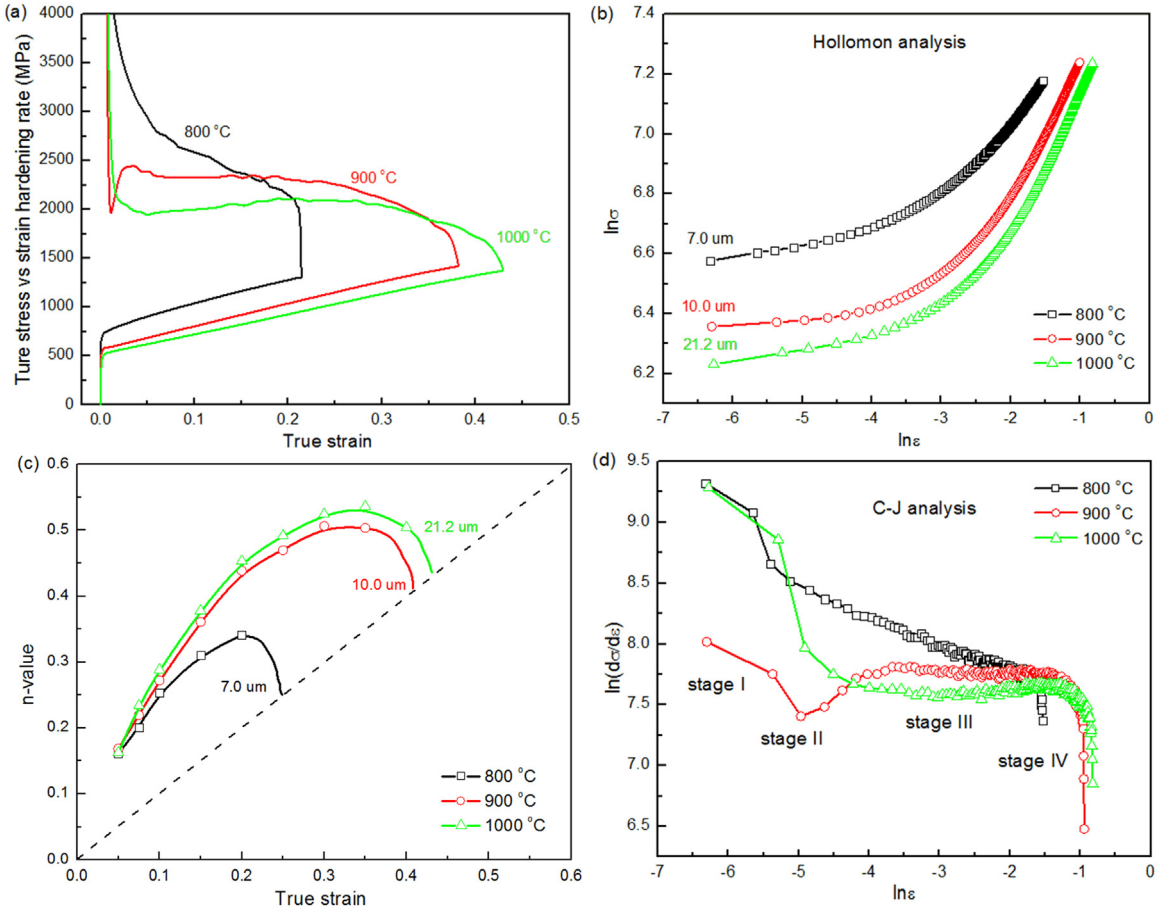

Fig. 13. True stress-strain curves and strain hardening rate-true strain curves of the investigated material.

4. Discussion

4.1. Strain hardening behavior

Fig. 13 shows the strain hardening behavior as a function of true strain for the annealed samples. The strain hardening rate is nearly around 2 GPa and maintains constant or slightly increases up to large strains, especially for state 900 and state 1000, rendering high strength and ductility to this recrystallized Fe-Mn-Al-C steel.

Generally, the strain hardening behaviors are characterized by the strain hardening exponent n, obtained from the true stress-true strain curve [55,56]. The most commonly used method to determine the n value is Hollomon analysis, as shown in Eq. (3).

$$\sigma = k\varepsilon^n \tag{3}$$

where σ is the true stress, ε is the true strain, k is a constant and n is the strain hardening exponent. The natural logarithmic form of differentiation with respect to ε in Eq. (3) is written as

$$\ln \sigma = n \ln \varepsilon + \ln k \tag{4}$$

where n is the slope of lnσ-lnε curve and ln$k$ is the related intercept.

The Hollomon analysis of the annealed samples is shown in Fig. 13b. Each lnσ-lnε curve has an upward curvature and none of them shows a linear lnσ- lnε relationship over the whole uniform strain ranges. The n value continuously increases with the increase in strain and the strength coefficient k decreases with the increase in austenite grain size. G. Dini et al. [38] also reported the similar results about the Fe-31Mn-3Al-3Si TWIP steel. These values of strain hardening exponent n are not constant like that of the conventional DP steels with a straight-line in the lnσ- lnε plot reported in ref. [57]. To reflect the change of n value with the strain, the instantaneous n_i value [58] is calculated to show the variations in the strain hardening behavior, depicted in Fig. 13c. The sample annealed at 1000 °C with the largest grain size of 21.2 μm has the highest n_i-values over the entire strain range and the n_i-value decreases with the reduction of austenite grain size. It is worth mentioning that a higher instantaneous n_i-value does not mean a higher strain hardening rate.

Compared with Hollomon analysis, Crussard-Jaoul (C-J) analysis can reveal clear distinction of strain hardening behavior with various plastic deformation mechanisms in different stages [59]. It is described as

$$\sigma = \sigma_0 + k\varepsilon^n \tag{5}$$

where σ is the true stress, σ_0 is the yield stress, ε is the true strain, k is a constant and n is the strain hardening exponent. The natural logarithmic form of differentiation with respect to ε in Eq. (5) is expressed as

$$\ln(d\sigma/d\varepsilon) = (n-1)\ln \varepsilon + \ln(nk) \tag{6}$$

where (n-1) is the slope of ln(dσ/dε)-lnε curve.

Fig. 13d shows the ln(dσ/dε)-lnε curves of the annealed samples by the C-J analysis. The curves show stage I, stage II, stage III and stage IV with different slopes. The deformation mechanism of the investigated steel here can be explained with dynamic slip band refinement (DSBR) proposed in ref. [22], as well as the "glide plane softening" hypothesis proposed in ref. [23] valid for the non-aged steel with high temperature recrystallization. The strain hardening exponent n first decreases after the onset of plastic deformation (stage I) due to the initiation of mobile dislocations, and then rapidly decreases (stage II) due to the saturation of dislocations fill-up on slip planes. After then, it slightly decreases (stage III) due to the newly formed slip bands and their interactions causing the refinement of the slip bands substructure, and finally

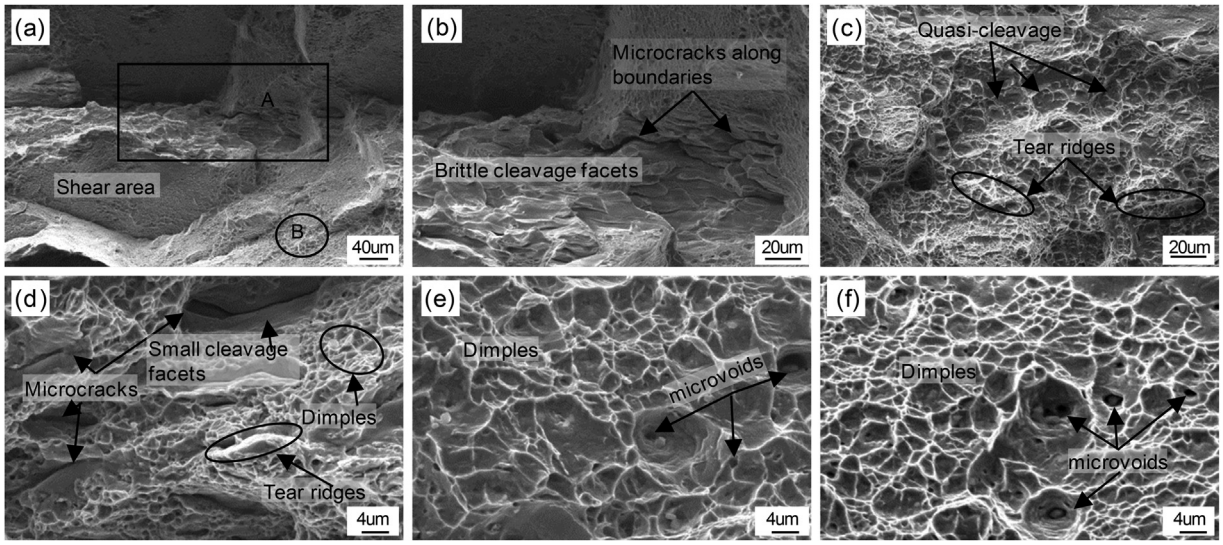

Fig. 14. SEM images of the fractured surface for the tensile samples with (a) cold-rolled state, (b) magnification of area A shown in (a), (c) magnification of area B shown in (a), (d) state 800, (e) state 900 and (f) state 1000.

decreases to fracture without obvious necking rapidly (stage IV). In addition, the smaller austenitic grain size is easier to fill up dislocations and faster to refine the slip bands substructure. Therefore, the strain hardening rate of state 800 with small grain size is higher than those of other samples with larger grain size. Consequently, the C-J analysis is better than Hollomon analysis deviated from linearity over the whole uniform strain range to explain the strain hardening behavior of the investigated steels.

4.2. Tensile toughness

The SEM images of fracture surface for tensile samples with different states are presented in Fig. 14. For cold-rolled state, the fracture surface is characterized by the presence of flat shear area flats and brittle cleavage facets (in Fig. 14a–b) and microcracks along boundaries (in Fig. 14b), as well as quasi-cleavage fracture including tear ridges (in Fig. 14c). Due to the grain boundary sliding [60], the shear flat surfaces with shallow dimples exhibit intergranular decohesion. The general tensile cleavage planes in FCC alloy are {001} planes [61], and result in the large shear area and brittle cleavage facets in Fig. 14a. The fracture of cold-rolled state is the typical brittle fracture mechanism. For state 800, the fracture surface consists of not only brittle fracture facets, microcracks, and quasi-cleavage fracture involving microvoid coalescence and tear ridges, but also many fine and shallow dimples, indicating locally brittle and ductile failure mechanisms. For state 900 and state 1000, the fracture surfaces are typical ductile fracture dominated by abundant dimples with various sizes, as shown in Fig. 14e–f. The size distribution of dimples for state 1000 is more even and deeper than that of state 900, which is related to the average grain size [41]. It indicates that the toughness of state 1000 is better than state 900. The inclusions of MnS, AlN, or Al_2O_3 located at the bottom of large dimples, shown in Fig. 14e–f, lead to decohesion between the particles and matrix during tensile deformation [62]. The interface between the brittle inclusions and austenite matrix has stress field, and easily form microvoids during the deformation process. With the increase of stress, the microvoids growth and coalescence lead to cracks formation and fracture.

The grain refinement not only influences the strength and elongation but also the toughness. Refined grains undertaking the external stress lead to small local stress concentration between intergranular and intragranular areas, which effectively hinder the initiation of cracks [63]. Due to the disordered atomic configuration areas, grain boundaries can effectively impede crack propagation into the adjacent grains, and can change the crack propagation direction with strain energy consumption when they go through the grain boundaries [50]. Refined grains provide more grain boundaries, thus it is beneficial to resist fracture and improve toughness. Although the average grain size of state 800 is the smallest, its fracture surface is brittle and ductile mixing mechanism. The reason is that the bimodal grain distribution is easier to generate local stress concentration, as well as the large κ-phase precipitated at the grain boundaries. The average austenitic grain size of state 900 is smaller than that of state 1000, but the toughness of the former one is less than that of the later one. From Fig. 8, the frequency of high misorientation angle for state 1000 is higher than that of state 900. It means that the refined austenite grain size is not the only factor to influence the tensile toughness, the frequency of high misorientation angle is also significant for the improvement of tensile toughness.

The tensile toughness is the ability to absorb energy for materials before rupturing, and it can be calculated by integrating the area under the engineering stress-strain curves up until fracture. The modulus of resilience is the area under the stress-strain curves up until yield point, and it is the elastic energy absorption per unit volume without plastic deformation. Fig. 15 presents the calculated results: the tensile toughness increases from 59 MJ/m^3 to 436 MJ/m^3 with the decrease in tensile strength from 1460 MPa to 890 MPa, and the related modulus of resilience decreases from 4.40 MJ/m^3 to 0.89 MJ/m^3 with the decrease in yield strength from 1218 MPa to 495 MPa. It indicates that large amount of deformation stress accumulated inside the material with high tensile strength is easier to crack and provide low plastic energy absorption, and the recrystallization behavior eliminates the deterioration effect and improves the fracture toughness at the expense of tensile strength. Conversely, the decrease in yield strength corresponds to low elastic toughness.

5. Conclusions

The recrystallization behavior of lightweight high-Mn high-Al steel with 50% cold rolling deformation has been investigated in this work. Comprehensive microstructure characterization is performed in the cold-rolled sample and samples annealed at different temperature to determine the austenite grain evolution and κ-phase precipitation behavior. The effect of grain size on tensile mechanical properties is analyzed. The strain hardening behavior and fracture toughness are discussed subsequently. The following conclusions are drawn:

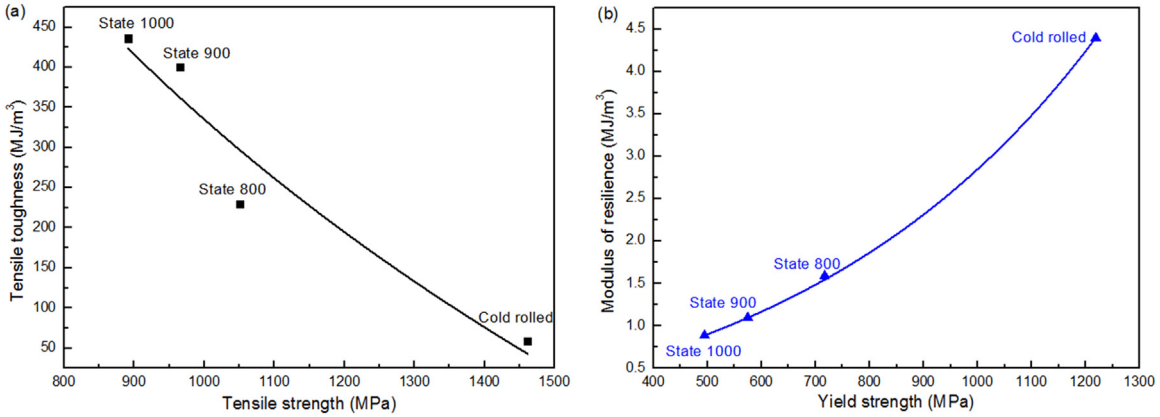

Fig. 15. (a) The relationship between tensile strength and tensile toughness, (b) the relationship between yield strength and modulus of resilience.

(1) The microstructure of the sample annealed at 800 °C is the partial recrystallized bimodal grains and κ-phase precipitates. Fully recrystallized austenite grains are obtained in the samples annealed at 900 °C and 1000 °C, and the grains grow with the increase in annealing temperature. The annealing twin boundaries effectively reduce the average austenitic grain size and the dispersity of austenite grain size.

(2) After recrystallization annealing, the strength reduces and elongation rises with the increase in annealing temperature. The steel annealed at 900 °C with fully recrystallized fine grains of 10.0 μm exhibits the optimum mechanical properties with excellent tensile strength of 965 MPa, ductility of 48.3% and good toughness of 400 MJ/m^3.

(3) The strain hardening rate continuously increases with the increasing of strain in the curves plotted by Hollomon analysis, and the C-J analysis is better to explain the strain hardening behavior of the investigated steels with various plastic deformation mechanisms in different four stages.

(4) The recrystallization behavior can improve the tensile toughness from 59 MJ/m^3 to 436 MJ/m^3 at the expense of tensile strength decrease from 1460 MPa to 890 MPa. Both the homogenous fine grains and high frequency of high misorientation angle generated from the recrystallization process are beneficial for the improvement of fracture toughness.

Acknowledgement

The authors gratefully acknowledge the financial supports from Deutsche Forschungsgemeinschaft (DFG) within Collaborative Research Centre SFB 761 'Steel - *ab initio*' (SFB 761), the China Scholarship Council (Grant No. 201506080057), and the National Science Foundation of China (Grant No. 51774083).

Data availability statement

The raw/processed data required to reproduce these findings cannot be shared at this time due to technical or time limitations.

References

[1] S.P. Chen, R. Rana, A. Haldar, R.K. Ray, Current state of Fe-Mn-Al-C low density steels, Prog. Mater. Sci. 89 (2017) 345–391.
[2] A.A. Saleh, E.V. Pereloma, A.A. Gazder, Texture evolution of cold rolled and annealed Fe-24Mn-3Al-2Si-1Ni-0.06C TWIP steel, Mater. Sci. Eng. A 528 (2011) 4537–4549.
[3] D. Raabe, H. Springer, I. Gutierrez-Urrutia, F. Roters, M. Bausch, J.-B. Seol, M. Koyama, P.-P. Choi, K. Tsuzaki, Alloy design, combinatorial synthesis, and microstructure-property relations for low-density Fe-Mn-Al-C austenitic steels, JOM 66 (2014) 1845–1856.
[4] I. Zuazo, B. Hallstedt, B. Lindahl, M. Selleby, M. Soler, A. Etienne, A. Perlade, D. Hasenpouth, V. Massardier-Jourdan, S. Cazottes, X. Kleber, Low-density steels: complex metallurgy for automotive applications, JOM 66 (2014) 1747–1758.
[5] H. Springer, D. Raabe, Rapid alloy prototyping: compositional and thermo-mechanical high throughput bulk combinatorial design of structural materials based on the example of 30Mn-1.2C-xAl triplex steels, Acta Mater. 60 (2012) 4950–4959.
[6] H. Kim, D.-W. Suh, N.J. Kim, Fe-Al-Mn-C lightweight structural alloys: a review on the microstructures and mechanical properties, Sci. Technol. Adv. Mater. 14 (2013) 1–11.
[7] I. Gutierrez-Urrutia, D. Raabe, High strength and ductile low density austenitic FeMnAlC steels: simplex and alloys strengthened by nanoscale ordered carbides, Mater. Sci. Tech. 30 (2014) 1099–1104.
[8] S.-H. Kim, H. Kim, N.J. Kim, Brittle intermetallic compound makes ultrastrong low-density steel with large ductility, Nature 518 (2015) 77–79.
[9] K.M. Chang, C.G. Chao, T.F. Liu, Excellent combination of strength and ductility in an Fe-9Al-28Mn-1.8C alloy, Scr. Mater. 63 (2010) 162–165.
[10] P.C. Chen, C.G. Chao, T.F. Liu, A novel high-strength, high-ductility and high-corrosion-resistance FeAlMnC low-density alloy, Scr. Mater. 68 (2013) 380–383.
[11] O. Acselrad, I.S. Kalashnikov, E.M. SILVA, M.S. Khadyev, R.A. Simao, Diagram of phase transformations in the austenite of hardened alloy Fe-28%Mn-8.5%Al-1%C-1.25%Si as a result of aging due to isothermal heating, Met. Sci. Heat. Treat. 48 (2006) 543–553.
[12] K. Choi, C.H. Seo, H. Lee, S.K. Kim, K.G. Chin, K.T. Park, N.J. Kim, Effect of aging on the microstructure and deformation behavior of austenite base lightweight Fe-28Mn-9Al-0.8C steel, Scr. Mater. 63 (2010) 1028–1031.
[13] I. Gutierrez-Urrutia, D. Raabe, Influence of Al content and precipitation state on the mechanical behavior of austenitic high-Mn low-density steels, Scr. Mater. 68 (2013) 343–347.
[14] Y. Kimura, K. Handa, K. Hayashi, Y. Mishima, Microstructure control and ductility improvement of the two-phase γ-Fe/κ-(Fe, Mn)3AlC alloys in the Fe-Mn-Al-C quaternary system, Intermetallics 12 (2004) 607–617.
[15] H. Huang, D. Gan, P.W. Kao, Effect of alloying additions on the κ phase precipitation in austenitic Fe-Mn-A1-C alloys, Scr. Metall. Mater. 30 (1994) 499–504.
[16] W.J. Lu, X.F. Zhang, R.S. Qin, κ-carbide hardening in a low-density high-Al high-Mn multiphase steel, Mater. Lett. 138 (2015) 96–99.
[17] W.W. Song, W. Zhang, J. von Appen, R. Dronskowski, W. Bleck, κ-phase formation in Fe-Mn-Al-C austenitic steels, Steel Res. Int. 85 (2015) 1–9.
[18] G. Frommeyer, U. Brüx, Microstructures and mechanical properties of high-strength Fe-Mn-Al-C light-weight TRIPLEX steels, Steel Res. Int. 77 (2006) 627–633.
[19] J.D. Yoo, K.T. Park, Microband-induced plasticity in a high Mn-Al-C light steel, Mater. Sci. Eng. A 496 (2008) 417–424.
[20] J.D. Yoo, S.W. Hwang, K.T. Park, Origin of extended tensile ductility of a Fe-28Mn-10Al-1C steel, Metall. Mater. Trans. A 40 (2009) 1520–1523.
[21] M.J. Yao, E. Welsch, D. Ponge, S.M.H. Haghighat, S. Sandlöbes, P. Choi, M. Herbig, I. Bleskov, T. Hickel, M. Lipinska-Chwalek, P. Shanthraj, C. Scheu, S. Zaefferer, B. Gault, D. Raabe, Strengthening and strain hardening mechanisms in a precipitation hardened high-Mn lightweight steel, Acta Mater. 140 (2017) 258–273.
[22] E. Welsch, D. Ponge, S.M. Hafez Haghighat, S. Sandlöbes, P. Choi, M. Herbig, S. Zaefferer, D. Raabe, Strain hardening by dynamic slip band refinement in a high-Mn lightweight steel, Acta Mater. 116 (2016) 188–199.
[23] C. Hasse, C. Zehnder, T. Ingendahl, A. Bikar, F. Tang, B. Hallstedt, W. Hu, W. Bleck, D.A. Molodov, On the deformation behavior of κ-carbide-free and κ-carbide-containing high-Mn light-weight steel, Acta Mater. 122 (2017) 332–343.
[24] W.C. Cheng, C.Y. Cheng, C.W. Hsu, D.E. Laughlin, Phase transformation of the $L1_2$ phase to kappa-carbide after spinodal decomposition and ordering in an Fe-C-Mn-Al austenitic steel, Mater. Sci. Eng. A 642 (2015) 128–135.
[25] K.-T. Park, K.G. Jin, S.H. Han, S.W. Hwang, K. Choi, C.S. Lee, Stacking fault energy and plastic deformation of fully austenitic high manganese steels: effect of Al addition, Mater. Sci. Eng. A 527 (2010) 3651–3661.
[26] J. Moon, S.-J. Park, J.H. Jang, T.-H. Lee, C.-H. Lee, H.-U. Hong, D.-W. Suh, S.H. Kim, H.N. Han, B.H. Lee, atomistic investigations of κ-carbide precipitation in austenitic Fe-Mn-Al-C lightweight steels and the effect of Mo addition, Scr. Mater. 127 (2017) 97–101.
[27] Z.Q. Wu, H. Ding, H.Y. Li, M.L.H.F.R. Cao, Microstructural evolution and strain

hardening behavior during plastic deformation of Fe-12Mn-8Al-0.8C steel, Mater. Sci. Eng. A 584 (2013) 150–155.
[28] I. Gutierrez-Urrutia, D. Raabe, Multistage strain hardening through dislocation substructure and twinning in a high strength and ductile weightreduced Fe–Mn–Al–C steel, Acta Mater. 60 (2012) 5791–5802.
[29] W.W. Song, T. Ingendahl, W. Bleck, Control of strain hardening behavior in high-Mn austenitic steels, Acta Metall. Sin. 27 (2014) 546–556.
[30] V. Rigaut, D. Daloz, J. Drillet, A. Perlade, P. Maugis, G. Lesoult, Phase equilibrium study in quaternary iron-rich Fe-Al-Mn-C alloys, ISIJ Int. 47 (2007) 898–906.
[31] J.-B. Seol, D. Raabe, P. Choi, H.-S. Park, J.-H. Kwak, C.-G. Park, Direct evidence for the formation of ordered carbides in a ferrite-based low-density Fe-Mn-Al-C alloy studied by transmission electron microscopy and atom probe tomography, Scr. Mater. 68 (2013) 348–353.
[32] Z.Q. Wu, H. Ding, X.H. An, D. Han, X.Z. Liao, Influence of Al content on the strain-hardening behavior of aged low density Fe-Mn-Al-C steels with high Al content, Mater. Sci. Eng. A 639 (2015) 187–191.
[33] L.F. Zhang, R.B. Song, C. Zhao, F.Q. Yang, Work hardening behavior involving the substructural evolution of a austenite-ferrite Fe-Mn-Al-C steel, Mater. Sci. Eng. A 640 (2015) 225–234.
[34] D. Canadinc, H. Sehitoglu, H.J. Maier, Y.I. Chumlyakov, Strain hardening behavior of aluminum alloyed Hadfield steel single crystals, Acta Mater. 53 (2005) 1831–1842.
[35] V. Gerold, H.P. Karnthaler, On the origin of planar slip in f.c.c. alloys, Acta Metall. 37 (1989) 2177–2183.
[36] R. Saha, R. Ueji, N. Tsuji, Fully recrystallized nanostructure fabricated without severe plastic deformation in high-Mn austenitic steel, Scr. Mater. 68 (2013) 813–816.
[37] A. Etienne, V. Massardier-Jourdan, S. Cazottes, X. Garat, M. Soler, I. Zuazo, X. Kleber, Ferrite effects in Fe-Mn-Al-C Triplex Steels, Metall. Mater. Trans. A 45A (2014) 324–334.
[38] G. Dini, A. Najafizadeh, R. Ueji, S.M. Monir-Vaghefi, Tensile deformation behavior of high manganese austenitic steel: the role of grain size, Mater. Des. 31 (2010) 3395–3402.
[39] R. Rana, C. Liu, R.K. Ray, Recrystallization in a low-density low-alloy Fe–Mn–Al–C duplex-phase alloy, Philos. Mag. Lett. 94 (3) (2014) 127–134.
[40] L. Bracke, K. Verbeken, L. Kestens, J. Penning, Recrystallization behaviour of an austenitic high Mn steel, Mater. Sci. Forum 558–559 (2007) 137–142.
[41] S. Kang, Y.-S. Jung, J.-H. Jun, Y.-K. Lee, Effects of recrystallization annealing temperature on carbide precipitation, microstructure, and mechanical properties in Fe-18Mn-0.6C-1.5Al TWIP steel, Mater. Sci. Eng. A 527 (2010) 745–751.
[42] C. Hasse, M. Kühbach, L.A. Barrales-Mora, S.L. Wong, F. Roters, D.A. Molodov, G.: Gottstein, Recrystallization behavior of a high-manganese steel: experiments and simulations, Acta Mater. 100 (2015) 155–168.
[43] A. Saeed-Akbari, L. Mosecker, A. Schwedt, W. Bleck, Characterization and prediction of flow behavior in high-manganesetwinning induced plasticity steels: part I. Mechanism maps and work-hardening behavior, Metall. Mater. Trans. A 5 (2012) 1688–1704.
[44] J.O. Andersson, T. Helander, L. Höglund, P. Shi, B. Sundman, Thermo-Calc & DICTRA, computational tools for materials science, Calphad 26 (2002) 273–312.
[45] M. Daamen, S. Richter, G. Hirt, Microstructure analysis of high-manganese TWIP steels produced via strip casting, Key Eng. Mater. 554–557 (2013) 553–561.
[46] R. Ueji, N. Tsuchida, D. Terada, N. Tsuji, Y. Tanaka, A. Takemura, K. Kunishige, Tensile properties and twinning behavior of high manganese austenitic steel with fine-grained structure, Scr. Mater. 59 (2008) 963–966.
[47] S. Yi, H.-G. Brokmeier, D. Letzig, Microstructural evolution during the annealing of an extruded AZ31 magnesium alloy, J. Alloy. Compd. 506 (2010) 364–371.
[48] M.F. Ashby, The deformation of plastically non-homogeneous materials, Philos. Mag. 21 (1970) 399–424.
[49] C. Castan, F. Montheillet, A. Perlade, Dynamic recrystallization mechanisms of an Fe-8%Al low density steel under hot rolling conditions, Scr. Mater. 68 (2013) 360–364.
[50] X.L. Zhang, Z.Q. Jiang, S.X. Li, J.W. Fan, Effect of effective grain size and grain boundary of large misorientation on upper shelf energy in pipeline steels, J. Wuhan Univ. Technol. 31 (2016) 606–610.
[51] C.M. Chu, H. Huang, P.W. Kao, D. Gan, Effect of alloying chemistry on the lattice constant of austenitic Fe-Mn-Al-C alloys, Scr. Metall. Mater. 30 (1994) 505–508.
[52] S.S. Babu, E.D. Specht, S.A. David, E. Karapetrova, P. Zschack, M. Peet, H.K.D.H. Bhadeschia, In-situ observations of lattice parameter fluctuations in austenite and transformation to bainite, Metall. Mater. Trans. A 36A (2005) 3281–3289.
[53] H.J. Stone, M.J. Peet, H.K.D.H. Bhadeshia, P.J. Withers, S.S. Babu, E.D. Specht, Synchrotron X-ray studies of austenite and bainitic ferrite, Proc. R. Soc. A 464 (2008) 1009–1027.
[54] Z.Y. Liang, Y.Z. Li, M.X. Huang, The respective hardening contributions of dislocations and twins to the flow stress of a twinning-induced plasticity steel, Scr. Mater. 112 (2016) 28–31.
[55] D. Barbier, N. Gey, S. Allain, N. Bozzolo, M. Humbert, Analysis of the tensile behavior of a TWIP steel based on the texture and microstructure evolutions, Mater. Sci. Eng. A 500 (2009) 196–206.
[56] Y.S. Jung, Y.K. Lee, Effect of pre-deformation on the tensile properties of a metastable austenitic steel, Scr. Mater. 59 (2008) 47–50.
[57] C.N. Li, F.Q. Ji, G. Yuan, J. Kang, R.D.K. Misra, G.D. Wang, The impact of the thermo-mechanical controlled processing on structure-property relationship and strain hardening behavior in dual phase steels, Mater. Sci. Eng. A 662 (2016) 100–110.
[58] A.K. Sachdev, Effect of retained austenite on the yielding and deformation behavior of a dual phase steel, Acta Metall. 31 (1983) 2037–2042.
[59] W.H. Zhang, J.L. Wu, Y.H. Wen, J.J. Ye, N. Li, Characterization of different work hardening behavior in ASI 321 stainless steel and Hadfield steel, J. Mater. Sci. 45 (2010) 3433–3437.
[60] K.R. Carpenter, R. Dippenaar, C.R. Killmore, Hot ductility of Nb- AND Ti-bearing microalloyed steels and the influence of thermal history, Mater. Metall. Trans. A 40 (2009) 573–580.
[61] R.L. Tobler, D. Meyn, Cleavage-like fracture along slip planes in Fe-18Cr-3Ni-13Mn-9.37N austenitic stainless steel at liquid helium temperature, Metal. Trans. A 19A (1988) 1626–1631.
[62] X. Sun, K.S. Choi, A. Soulami, W.N. Liu, M.A. Khaleel, On key factors influencing ductile fractures of dual phase (DP) steels, Mater. Sci. Eng. A 526 (2009) 140–149.
[63] F.Q. Ji, C.N. Li, S. Tang, G. Yuan, G.D. Wang, Microstructural characteristics with various finish rolling temperature and low temperature toughness in hot rolled Nb-Ti ferritic steel, ISIJ Int. 56 (2016) 602–609.